



# Chemical Evolution of Isotopically Labeled Carbon Dioxide ( $^{13}\text{CO}_2$ ) Ice Exposed to Ionizing Radiation and Implications for Trans-Neptunian Objects

Chaojiang Zhang<sup>1,2</sup> , Leslie A. Young<sup>3</sup> , and Ralf I. Kaiser<sup>1,2</sup>

<sup>1</sup> W. M. Keck Research Laboratory in Astrochemistry, University of Hawaii at Manoa, Honolulu, HI 96822, USA; ralfk@hawaii.edu

<sup>2</sup> Department of Chemistry, University of Hawaii at Manoa, Honolulu, HI 96822, USA

<sup>3</sup> Department of Space Studies, Southwest Research Institute, Boulder, CO 80302, USA

Received 2024 October 7; revised 2024 December 2; accepted 2025 January 12; published 2025 February 19

## Abstract

We present results on the radiation chemistry of isotopically labeled carbon dioxide ( $^{13}\text{CO}_2$ ) ices induced by energetic electrons at 40 and 10 K to simulate the chemical evolution of carbon dioxide on trans-Neptunian objects exposed to galactic cosmic-ray particles. By collecting infrared spectra during the irradiation of  $^{13}\text{CO}_2$  ices, we have identified several radiolysis products, including carbon monoxide ( $^{13}\text{CO}$ ), ozone ( $\text{O}_3$ ), carbon trioxide ( $^{13}\text{CO}_3$ ) with cyclic ( $C_{2v}$ ) and acyclic ( $D_{3h}$ ) isomers, carbon tetraoxide ( $^{13}\text{CO}_4$ ), carbon pentaoxide ( $^{13}\text{CO}_5$ ), and carbon hexaoxide ( $^{13}\text{CO}_6$ ). The temporal profiles reveal that all products exhibit a rapid increase followed by a gradual decrease during prolonged irradiation, with the reduction at 40 K occurring faster than at 10 K. Furthermore, the ratio of  $^{13}\text{CO}$  to  $^{13}\text{CO}_2$  rises to constants of 0.20 at 40 K and 0.27 at 10 K as radiation accumulates within ices, which has potential implications for understanding the specific conditions of trans-Neptunian objects, such as galactic cosmic-ray exposure history, or other astrophysical scenarios characterized by abundant carbon dioxide.

*Unified Astronomy Thesaurus concepts:* Carbon dioxide (196); Laboratory astrophysics (2004); Trans-Neptunian objects (1705); Surface ices (2117); Surface composition (2115)

## 1. Introduction

Carbon dioxide ( $\text{CO}_2$ ) and isotopically labeled molecules ( $^{13}\text{CO}_2$ ) have been identified ubiquitously in the trans-Neptunian space by the James Webb Space Telescope (JWST; M. E. Brown & W. C. Fraser 2023; M. N. De Prá et al. 2024; J. P. Emery et al. 2024; A. C. Souza-Feliciano et al. 2024). Along with the solar system ices,  $\text{CO}_2$  represents one of the dominant components in interstellar ices with abundances of 10%–40% relative to water ( $\text{H}_2\text{O}$ ; L. B. D'Hendecourt et al. 1989; S. Ioppolo et al. 2013b; A. C. A. Boogert et al. 2015; S. L. Grant et al. 2023; M. K. McClure et al. 2023; N. G. C. Brunken et al. 2024; O. Nayak et al. 2024; J. A. Noble et al. 2024). The solid-state formation of  $\text{CO}_2$  in these icy mantles is thought to be resulting from both energetic and nonenergetic pathways under astrophysical conditions such as ground-state carbon monoxide (CO) interacting with an electronically excited  $\text{CO}^*$  (C. S. Jamieson et al. 2006c; C. J. Bennett et al. 2009a, 2010); the reaction between condensed CO and hydroxyl ( $\text{OH}$ ) radical through a HOCO intermediate (Y. Oba et al. 2010; E.-L. Zins et al. 2011; C. Yuan et al. 2014; G. Molpeceres et al. 2023; A. Ishibashi et al. 2024); CO reacting with atomic oxygen (M. Minissale et al. 2013; S. Ioppolo et al. 2013a); formaldehyde ( $\text{H}_2\text{CO}$ ) reacting with atomic oxygen (M. Minissale et al. 2015); or ionizing radiation-processed water-covered carbonaceous grains (V. Mennella et al. 2004; O. Gomis & G. Strazzulla 2005; V. Mennella et al. 2006; D. Fulvio et al. 2012; U. Raut et al. 2012; T. Sabri et al. 2015). The  $\text{CO}_2$  ice in astrophysical environments has been mostly observed via the asymmetric stretching mode ( $\nu_3$ ) at  $4.26 \mu\text{m}$  ( $\sim 2347 \text{ cm}^{-1}$ )

accompanied by the corresponding vibration of  $^{13}\text{CO}_2$  at  $\sim 4.39 \mu\text{m}$  ( $\sim 2278 \text{ cm}^{-1}$ ) and the bending mode ( $\nu_2$ ) at  $\sim 15.2 \mu\text{m}$  ( $\sim 660 \text{ cm}^{-1}$ ) (S. Ioppolo et al. 2013b; M. E. Brown & W. C. Fraser 2023; N. G. C. Brunken et al. 2024). Additional combination modes of  $\nu_1 + \nu_3$  and  $2\nu_2 + \nu_3$  located at about 2.70 and  $2.78 \mu\text{m}$  ( $\sim 3704$  and  $\sim 3597 \text{ cm}^{-1}$ ) have also been observed on trans-Neptunian objects (TNOs), toward protostellar objects, and molecular clouds (J. V. Keane et al. 2001; M. K. McClure et al. 2023; M. N. De Prá et al. 2024; J. A. Noble et al. 2024; A. C. Souza-Feliciano et al. 2024). The symmetric stretching mode ( $\nu_1$ ) is inactive in the infrared region. A shoulder band at  $\sim 2329 \text{ cm}^{-1}$  appears in the laboratory spectrum of pure  $\text{CO}_2$  ice and can be assigned to the amorphous phase, but this feature has not been apparent in astronomical observations, suggesting that the structure of pure  $\text{CO}_2$  ice in space is possibly dominated by the crystalline phase (R. M. Escribano et al. 2013; M. A. Allodi et al. 2014; P. A. Gerakines & R. L. Hudson 2015). In addition, the  $\nu_1 + \nu_3$  mode has also been proposed to quantify the degree of crystallinity of  $\text{CO}_2$  within interstellar ice (J. He & G. Vidali 2018; J. He et al. 2018).

Laboratory studies have demonstrated that the infrared absorption profiles of  $\text{CO}_2$ -containing ice mixtures strongly correlate with the physical and chemical environment such as radiation exposure accumulation, temperature, and ice components (P. Ehrenfreund et al. 1997; K. I. Öberg et al. 2006; K. I. Öberg et al. 2009; R. M. Escribano et al. 2013; K. Isokoski et al. 2013; S. Jheeta 2014; I. R. Cooke et al. 2016; G. A. Baratta & M. E. Palumbo 2017; A. B. Hacquard et al. 2024). Since the JWST has determined widespread  $\text{CO}_2$  on TNOs, this molecule naturally becomes an outstanding candidate for tracing the properties of the outer solar system, such as the thermal and radiation exposure history and carbon source on the surface of carbon-rich objects (R. J. Cartwright et al. 2022; S. K. Trumbo & M. E. Brown 2023; G. L. Villanueva et al. 2023; R. J. Cartwright et al. 2024a; S. Faggi et al. 2024). The  $\nu_3$  asymmetric stretch and



Original content from this work may be used under the terms of the [Creative Commons Attribution 4.0 licence](#). Any further distribution of this work must maintain attribution to the author(s) and the title of the work, journal citation and DOI.

$\nu_2$  bending modes often suffer from saturation and are highly susceptible to the shape and size of objects, which distorts the appearance of the absorption band (E. Dartois et al. 2022). Alternatively, the  $^{13}\text{CO}_2$  stretching mode at  $\sim 2278 \text{ cm}^{-1}$  is often used as a proxy to study the characteristics of  $\text{CO}_2$  in space (A. C. A. Boogert et al. 2000; S. L. Grant et al. 2023; N. G. C. Brunken et al. 2024). In addition, since the majority of outer solar system icy bodies are exposed to energetic particles from the solar winds (SWs) or galactic cosmic rays (GCRs; R. E. Johnson, 1990; R. I. Kaiser & K. Roessler 1997; C. J. Bennett et al. 2013), a complex suite of products generated from ionizing radiation-processed  $\text{CO}_2$  ices is expected to be detectable such as carbon monoxide, ozone, carbon trioxide, and higher-order carbon oxides (R. I. Kaiser & A. M. Mebel 2008; U. Raut & R. A. Baragiola 2013; B. Sivaraman et al. 2013; C. J. Bennett et al. 2014; H. Carrascosa et al. 2019; N. E. Sie et al. 2019; B. C. Ferrari et al. 2021; D. V. Mifsud et al. 2022). Simultaneously, the only CO detection on those TNOs having a higher abundance of  $\text{CO}_2$  suggests a potential CO formation mechanism from the irradiation processing of  $\text{CO}_2$  ices (M. N. De Prá et al. 2024). Considering the typical temperature range of TNOs is 30–50 K, higher than the sublimation point of CO, this molecule is likely to be trapped in more stable compounds like the residues from ionizing radiation-processed methanol (C. S. Jamieison et al. 2006c; L. A. Young et al. 2020; M. E. Brown & W. C. Fraser 2023; E. Quirico et al. 2023; S. P. D. Birch & O. M. Umurhan 2024; C. Zhang et al. 2024). The ionizing radiation exposure on isotopically labeled carbon dioxide ( $^{13}\text{CO}_2$ ) and mixing with products will significantly modify their spectral signatures but underlying chemical evolution has remained elusive.

Here, we present a comprehensive study on the chemical evolution of  $^{13}\text{CO}_2$  ice processed by high-energy electrons to mimic the ionizing radiation exposure on small TNOs (W. Zheng et al. 2008; Y. S. Kim & R. I. Kaiser 2012; B. M. Jones & R. I. Kaiser 2013; N. F. Kleimeier et al. 2022). The highly energetic electrons simulate the secondary electrons formed in the track of GCRs penetrating the TNO surface ices; the interaction between these electrons and molecules essentially controls the chemical reactions within the icy mantles and induces modification of the spectroscopically probed ice layers (R. E. Johnson, 1990; C. J. Bennett et al. 2005). The processing temperature of  $^{13}\text{CO}_2$  ices is kept at 40 and 10 K, which coincides with the typical surface temperature of TNOs (L. A. Young et al. 2020; S. M. Menten et al. 2022). This study measured the position of a series of isotopically labeled carbon oxide products, and their formation pathways are discussed by combining kinetic profiles. During prolonged irradiation, the ratio between  $^{13}\text{CO}$  and  $^{13}\text{CO}_2$  rapidly reaches constant values of 0.20 and 0.27 at 40 and 10 K. The data obtained here provide fundamental information for enabling a thorough exploration of  $^{13}\text{CO}_2$  ice behaviors when exposed to radiation environments and potentially detectable isotopically labeled carbon oxide products on the surface of TNOs, as well as the use of the carbon monoxide–carbon dioxide ratio as a clock of determining the radiation chemistry on the surfaces of TNOs.

## 2. Experimental Methods

The irradiation experiments are performed in an ultrahigh vacuum chamber at a pressure of about  $4 \times 10^{-11}$  Torr, which has been described in detail elsewhere (M. J. Abplanalp et al. 2016;

**Table 1**  
Data Were Applied to Calculate the Irradiation Dose in the Carbon Dioxide ( $^{13}\text{CO}_2$ ) Ices

Parameter	Value
Initial kinetic energy of the electrons, $E_{\text{init}}$ (keV)	5
Ices	$^{13}\text{CO}_2$
Irradiation current, $I$ (nA)	$1400 \pm 120$
Total number of electrons	$3.37 \times 10^{17}$
Average penetration depth, $l$ (nm) <sup>a</sup>	$281 \pm 30$
Average kinetic energy of backscattered electrons, $E_{\text{bs}}$ (eV) <sup>a</sup>	$3610 \pm 320$
Fraction of backscattered electrons, $f_{\text{bs}}^{\text{a}}$	$0.46 \pm 0.03$
Average kinetic energy of transmitted electrons, $E_{\text{trans}}$ (eV) <sup>a</sup>	0
Fraction of transmitted electrons, $f_{\text{trans}}^{\text{a}}$	0
Irradiated area, $A$ (cm <sup>2</sup> )	$1 \pm 0.05$
Dose (eV molecule <sup>-1</sup> )	$3684 \pm 320$
Dose (eV amu <sup>-1</sup> )	$82 \pm 10$

**Note.**

<sup>a</sup> Parameters are obtained from CASINO software v2.4.

A. M. Turner & R. I. Kaiser 2020). In the chamber, a polished silver wafer is attached to an oxygen-free high conductivity copper target via indium foil. The copper target is connected to a two-stage closed-cycle helium refrigerator (CTI-Cryogenics Cryodyne 1020, compressor: CTI-Cryogenics 9600) to generate cryogenic temperature; the latter was monitored by a silicon diode sensor (Lakeshore DT-470) and regulated in a range of 5–320 K by a programmable temperature controller (Lakeshore 336). When the substrate is cooled down to  $5.5 \pm 0.3$  K, carbon- $^{13}\text{C}$  dioxide ( $^{13}\text{CO}_2$ , Airgas, 99.999%) will be deposited onto the substrate via a glass capillary array. Based on the refractive index ( $n$ ) of  $1.30 \pm 0.02$  for solid  $\text{CO}_2$  (M. Bouilloud et al. 2015; P. A. Gerakines & R. L. Hudson 2015), the thicknesses of deposited  $^{13}\text{CO}_2$  ices were determined to be  $850 \pm 50$  nm by monitoring the reflected power with a helium-neon laser (CVI Melles-Griot, 25-LHP-230, 632.8 nm) at a  $4^\circ$  angle of incidence (A. M. Turner et al. 2015). After deposition,  $^{13}\text{CO}_2$  ices were heated to 10 or 40 K, and isothermally processed by 5 keV electrons (Specs EQ 22/35 electron source) to simulate the secondary electrons formed in the track of GCR penetrating TNO surfaces (R. E. Johnson 1991; C. J. Bennett et al. 2005). The electron beam has an incidence angle of  $70^\circ$  to the ice surface normal. Utilizing Monte Carlo simulations (CASINO 2.42; D. Drouin et al. 2007), the electrons have an average depth of  $281 \pm 30$  nm. The maximum depth of the electrons is calculated to be  $550 \pm 50$  nm, which is less than the ice thickness of  $850 \pm 50$  nm, thus avoiding interaction between electrons and the surface of the silver wafer. The radiation dose deposited into the  $^{13}\text{CO}_2$  ices is controlled to be  $82 \pm 10$  eV amu<sup>-1</sup> (Table 1). The  $^{13}\text{CO}_2$  ices along with radiolysis products are analyzed in situ by a Fourier transform infrared (FTIR) spectrometer (Thermo Fisher Scientific, Nicolet 6700 Spectrometer, liquid nitrogen cooled MCTB detector). The FTIR spectrometer is operated in an absorption-reflection-absorption mode with a reflection angle of  $45^\circ$  and monitors the infrared electromagnetic waves in the range of  $6000$ – $650 \text{ cm}^{-1}$  in the resolution of  $4 \text{ cm}^{-1}$ . Each infrared spectrum is collected for 2 minutes (220 scans) to minimize the influence of noise signals. A background spectrum is measured before depositing  $^{13}\text{CO}_2$  and subtracted during the collection of infrared spectra. To determine the amounts of molecules and plot the temporal profiles during irradiation of  $^{13}\text{CO}_2$ , we integrate numerous absorptions and calculate their column density (i.e., the

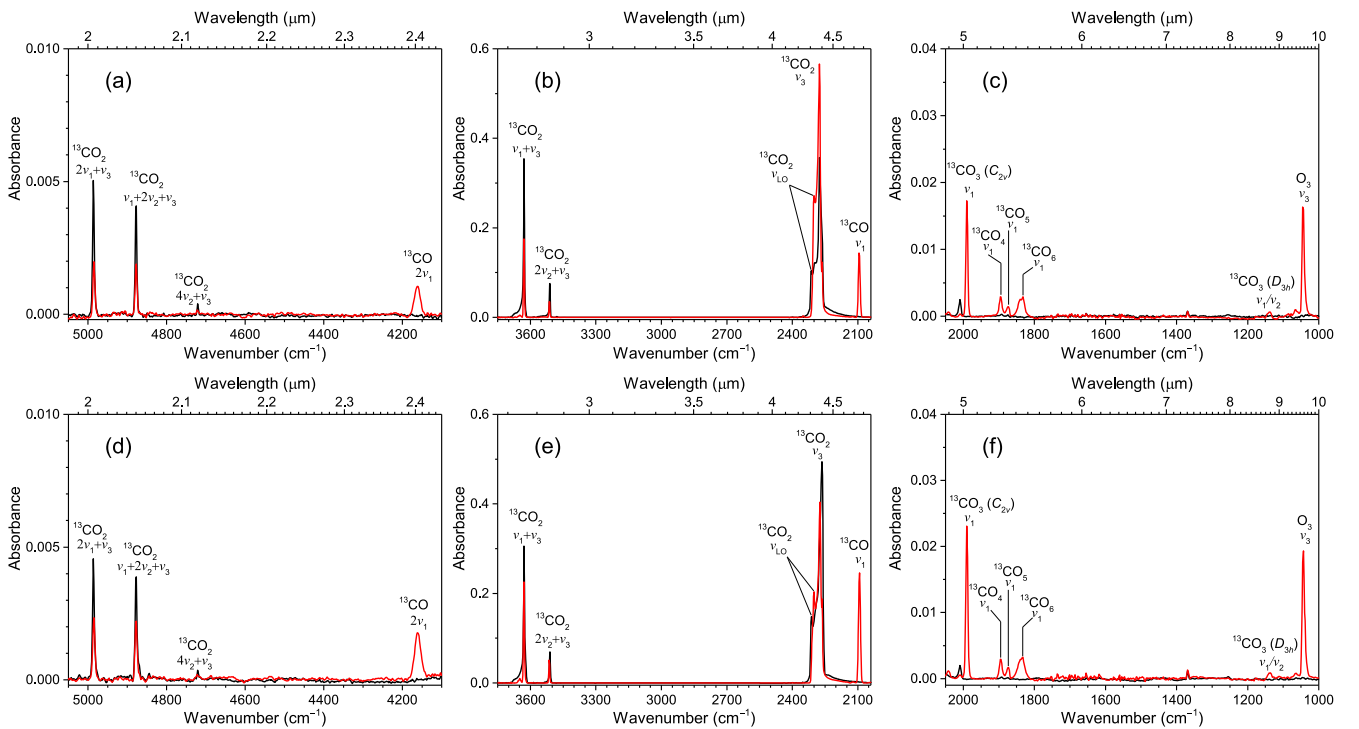


**Figure 1.** Infrared spectra of carbon dioxide ( $^{13}\text{CO}_2$ ) ices before irradiation (black line) and after irradiation (red line) at 40 (upper) and 10 K (lower) shown over several different wavelength ranges of  $5050\text{--}4100\text{ cm}^{-1}$ ,  $3750\text{--}2050\text{ cm}^{-1}$ , and  $2050\text{--}1000\text{ cm}^{-1}$ .

number of absorbing molecules per  $\text{cm}^2$ ) through a modified Lambert–Beer relationship (P. B. Crandall et al. 2019).

### 3. Results and Discussion

#### 3.1. Infrared Absorption Band Assignments

The infrared spectra of  $^{13}\text{CO}_2$  ices before and after irradiation at 40 and 10 K are shown in Figure 1. To clearly show observed absorptions, only the spectra of three regions with signals are presented:  $5050\text{--}4100\text{ cm}^{-1}$ ,  $3750\text{--}2050\text{ cm}^{-1}$ , and  $2050\text{--}1000\text{ cm}^{-1}$ . Band positions and assignments are listed in Table 2. Overall, the spectra of pristine  $^{13}\text{CO}_2$  ices are dominated by the fundamental vibration  $\nu_3$  mode between  $2340$  and  $2240\text{ cm}^{-1}$  along with the combination modes at  $3511\text{ cm}^{-1}$  ( $2\nu_2 + \nu_3$ ),  $3629\text{ cm}^{-1}$  ( $\nu_1 + \nu_3$ ),  $4721\text{ cm}^{-1}$  ( $4\nu_2 + \nu_3$ ),  $4878\text{ cm}^{-1}$  ( $\nu_1 + 2\nu_2 + \nu_3$ ), and  $4987\text{ cm}^{-1}$  ( $2\nu_1 + \nu_3$ ). Several weak peaks associated with overtone  $2\nu_2$  at  $1368\text{ cm}^{-1}$ , Fermi resonances located at  $2009\text{ cm}^{-1}$  (V. Rodriguez-Garcia et al. 2007), and  $\nu_3$  mode of  $\text{CO}_2$  at  $2352\text{ cm}^{-1}$  are also detected. Each of the peaks in Table 2 is in good agreement with previous reports (W. E. Osberg & D. F. Hornig 1952; M. Falk 1987; S. A. Sandford & L. J. Allamandola 1990; P. A. Gerakines et al. 1996; P. Ehrenfreund et al. 1997; M. Bernstein et al. 2005; K. I. Öberg et al. 2009; K. Isokoski et al. 2013; C. J. Bennett et al. 2014; P. A. Gerakines & R. L. Hudson 2015; H. Carrascosa et al. 2019). In the  $\nu_3$ -region ( $2340\text{--}2240\text{ cm}^{-1}$ ), the longitudinal optical (LO) mode at  $2312\text{ cm}^{-1}$  is detected due to an incident light angle of  $45^\circ$  used in this study (M. A. Ovchinnikov & C. A. Wight 1993; B. Maté et al. 2008; R. M. Escribano et al. 2013; C. Yuan & J. T. Yates 2013; I. R. Cooke et al. 2016; G. A. Baratta & M. E. Palumbo 1998, 2017; J. Vogt 2024). A splitting of  $37\text{ cm}^{-1}$  mirrored the previously reported value of  $39\text{ cm}^{-1}$  for  $\text{CO}_2$  ice at  $28\text{ K}$  using an incident light angle of  $40^\circ$  (I. R. Cooke et al. 2016). The presence of both crystalline  $^{13}\text{CO}_2$

centered at  $2275\text{ cm}^{-1}$  and amorphous  $^{13}\text{CO}_2$  centered at  $2264\text{ cm}^{-1}$  suggests that the deposited ices are mixtures of crystalline and amorphous  $^{13}\text{CO}_2$  (R. M. Escribano et al. 2013; P. A. Gerakines & R. L. Hudson 2015).

Upon irradiation, new absorption features emerged; these are assigned to radiolysis products including carbon monoxide ( $^{13}\text{CO}$ ), carbon trioxide ( $^{13}\text{CO}_3$ ) with cyclic ( $C_{2v}$ ) and acyclic ( $D_{3h}$ ) isomers, carbon tetraoxide ( $^{13}\text{CO}_4$ ), carbon pentaoxide ( $^{13}\text{CO}_5$ ), carbon hexaoxide ( $^{13}\text{CO}_6$ ), and ozone ( $O_3$ ) (C. J. Bennett et al. 2004; C. S. Jamieson et al. 2006a; C. S. Jamieson et al. 2007a, 2007b, 2008; K. I. Öberg et al. 2009; U. Raut & R. A. Baragiola 2013; B. Sivaraman et al. 2013; C. J. Bennett et al. 2014; R. Martín-Doménech et al. 2015; C. Mejía et al. 2015; N. E. Sie et al. 2019; D. V. Mifsud et al. 2022; A. B. Hacquard et al. 2024). Since carbon monoxide is volatile at  $40\text{ K}$ , the carbon monoxide detected here is trapped in the ices (C. S. Jamieson et al. 2006c). The absorptions of isotopically labeled carbon trioxide ( $^{13}\text{CO}_3$ ;  $C_{2v}/D_{3h}$ ), carbon tetraoxide ( $^{13}\text{CO}_4$ ), carbon pentaoxide ( $^{13}\text{CO}_5$ ), and carbon hexaoxide ( $^{13}\text{CO}_6$ ) appear at  $1990/1136\text{ cm}^{-1}$ ,  $1895\text{ cm}^{-1}$ ,  $1874\text{ cm}^{-1}$ , and  $1832\text{ cm}^{-1}$ , respectively. In addition, the frequency of LO mode presents a redshift from  $2313$  to  $2300\text{ cm}^{-1}$  at  $40\text{ K}$  and from  $2312$  to  $2301\text{ cm}^{-1}$  at  $10\text{ K}$ , which might be due to the formation of  $^{13}\text{CO}$  and  $O_2$  (I. R. Cooke et al. 2016). Although the  $O_2$  molecule is inactive in infrared spectra and unconfirmed in this work, it has been identified from the processed  $\text{CO}_2$  ice by a quadrupole mass spectrometer (B. Sivaraman et al. 2013; R. Martín-Doménech et al. 2015; H. Carrascosa et al. 2019; N. E. Sie et al. 2019). The evolution of the LO shift is plotted in Figure 2. At  $40\text{ K}$ , this shift increases rapidly to  $6\text{ cm}^{-1}$  in the first hour, then climbs to  $13\text{ cm}^{-1}$ . At  $10\text{ K}$ , it increases to  $8\text{ cm}^{-1}$  in the first hour and then slowly rises to  $11\text{ cm}^{-1}$ .

**Table 2**  
Infrared Absorption Assignments of Carbon Dioxide ( $^{13}\text{CO}_2$ ) Ices before and after Irradiation at 40 and 10 K

Before Irradiation			
Position (cm $^{-1}$ )		Assignment	References
40 K	10 K		
4987	4987	$2\nu_1 + \nu_3$ ( $^{13}\text{CO}_2$ )	(1)
4878	4878	$\nu_1 + 2\nu_2 + \nu_3$ ( $^{13}\text{CO}_2$ )	(1)
4721	4721	$4\nu_2 + \nu_3$ ( $^{13}\text{CO}_2$ )	(1)
3629	3629	$\nu_1 + \nu_3$ ( $^{13}\text{CO}_2$ )	(1), (2), (3)
3511	3510	$2\nu_2 + \nu_3$ ( $^{13}\text{CO}_2$ )	(1), (2), (3)
2353	2352	$\nu_3$ ( $\text{CO}_2$ )	(1), (2), (3)
2313	2312	$\nu_{\text{LO}}$ ( $^{13}\text{CO}_2$ ) <sup>a</sup>	(4), (5)
2275	...	$\nu_3$ ( $^{13}\text{CO}_2$ ) Crystalline	(5), (6)
...	2264	$\nu_3$ ( $^{13}\text{CO}_2$ ) Amorphous	(5), (6)
2009	2009	$\nu_{\text{Fermi}}$ ( $^{13}\text{CO}_2$ ) <sup>a</sup>	(2)
1368	1368	$2\nu_2$ ( $^{13}\text{CO}_2$ )	(1), (2), (3)
~658	~658	$\nu_2$ ( $^{13}\text{CO}_2$ )	(1), (2), (3)

After Irradiation			
Position (cm $^{-1}$ )		Assignment	References
40 K	10 K		
4985	4985	$2\nu_1 + \nu_3$ ( $^{13}\text{CO}_2$ )	(1)
4878	4878	$\nu_1 + 2\nu_2 + \nu_3$ ( $^{13}\text{CO}_2$ )	(1)
4722	4722	$4\nu_2 + \nu_3$ ( $^{13}\text{CO}_2$ )	(1)
4161	4160	$2\nu_1$ ( $^{13}\text{CO}$ )	(2), (3)
3630	3630	$\nu_1 + \nu_3$ ( $^{13}\text{CO}_2$ )	(1), (2), (3)
3513	3513	$2\nu_2 + \nu_3$ ( $^{13}\text{CO}_2$ )	(1), (2), (3)
2350	2350	$\nu_3$ ( $\text{CO}_2$ )	(1), (2), (3)
2300	2301	$\nu_{\text{LO}}$ ( $^{13}\text{CO}_2$ ) <sup>a</sup>	(4), (5)
2276	2274	$\nu_3$ ( $^{13}\text{CO}_2$ ) Crystalline	(5), (6)
2264	2264	$\nu_3$ ( $^{13}\text{CO}_2$ ) Amorphous	(5), (6)
2094	2092	$\nu_1$ ( $^{13}\text{CO}$ )	(2), (3)
1990	1990	$\nu_1$ ( $C_{2v}$ , $^{13}\text{CO}_3$ )	(2), (3)
1895	1895	$\nu_1$ ( $^{13}\text{CO}_4$ )	(2)
1873	1874	$\nu_1$ ( $^{13}\text{CO}_5$ )	(2)
1840	1841	$\nu_{\text{Fermi}}$ ( $^{13}\text{CO}_3$ ) <sup>a</sup>	(2)
1832	1832	$\nu_1$ ( $^{13}\text{CO}_6$ )	(2)
1369	1369	$2\nu_2$ ( $^{13}\text{CO}_2$ )	(1), (2), (3)
1136	1136	$\nu_1/\nu_2$ ( $D_{3h}$ , $^{13}\text{CO}_3$ )	(2)
1044	1044	$\nu_3$ ( $\text{O}_3$ )	(2), (3)

**Notes.** References. (1) M. Bernstein et al. (2005); (2) C. J. Bennett et al. (2014); (3) H. Carrascosa et al. (2019); (4) I. R. Cooke et al. (2016); (5) R. M. Escribano et al. (2013); (6) P. A. Gerakines and R. L. Hudson (2015).

<sup>a</sup> LO and Fermi indicate longitudinal optical and Fermi resonance, respectively.

### 3.2. Chemical Evolution and Reaction Mechanism

After identifying the products of  $^{13}\text{CO}$ ,  $\text{O}_3$ , and high-order carbon oxides ( $^{13}\text{CO}_x$ ,  $x > 2$ ), we will then trace their chemical evolution and discuss the possible reaction mechanism within  $^{13}\text{CO}_2$  ices initiated by GCR proxies. Figure 3 depicts the temporal profiles of each species identified in the infrared spectra. The absorption coefficients used for computing column densities are listed in Table 3. The laboratory processing time of TNO ice analogs can be scaled to the corresponding time of exposure experienced by a TNO surface (J. F. Cooper et al. 2003; G. Strazzulla et al. 2003; R. Hudson et al. 2008). This provides the potential to reconstruct the chemical evolution

from carbon-dioxide-rich TNO surface bombarded by GCRs and to relate the laboratory scale to the actual solar system timescale. Figure 3(a) reveals that  $^{13}\text{CO}_2$  ices at 40 and 10 K dissociate rapidly; 35% of the original  $^{13}\text{CO}_2$  is destroyed in the first 2 hr with faster damage at 10 K, possibly due to higher fractions of amorphous  $^{13}\text{CO}_2$  at 10 K; alternatively, a higher temperature of 40 K promotes an enhanced back-reaction and recycling of  $^{13}\text{CO}_2$ . As the irradiation time increases, the consumption of  $^{13}\text{CO}_2$  at 40 K gradually rises to 59% during the next 8 hr. However, it only increases to 42% at 10 K, suggesting the decay at 10 K is slower in this system. This differs from the previous report on  $\text{CO}_2$  ices processed by 1 keV electrons, which indicated that this decay occurs more rapidly with increasing temperature during the whole radiation period, and depletes about 55% of  $\text{CO}_2$  at 40 K (D. V. Mifsud et al. 2022). The primary product  $^{13}\text{CO}$  rapidly increases in the first hour and then drops off to  $4.3 \times 10^{16}$  and  $8.1 \times 10^{16}$  molecule cm $^{-2}$  at 40 and 10 K (Figure 3(b)); this accounts for about 13.8% and 36.4% of the consumed  $^{13}\text{CO}_2$  (Table 3). This decline may have been due to the prolonged irradiation inducing further dissociation of  $^{13}\text{CO}$  or the suprathermal oxygen atom promoting the recombination reaction forming back  $^{13}\text{CO}_2$  (C. S. Jamieson et al. 2006c; C. J. Bennett et al. 2009b; C. J. Bennett et al. 2014; M. Förstel et al. 2016). The abundance of the  $^{13}\text{CO}$  product at 10 K is about twice at 40 K because the dissociation of carbon monoxide at a higher temperature is more efficient (C. Zhang et al. 2024). Furthermore, the ratio between  $^{13}\text{CO}$  and  $^{13}\text{CO}_2$  increases to constant values of 0.20 at 40 K and 0.27 at 10 K as the radiation dose exceeds 18 eV amu $^{-1}$  (Figure 4). This dose is higher than that at which the  $\text{CO}:\text{CO}_2$  ratio reaches a constant of the  $\text{CO}:\text{CO}_2$  ratio (M. A. Satorre et al. 2000). The irradiated  $^{13}\text{CO}_2$  ice can trap volatile  $^{13}\text{CO}$  up to 20% even at 40 K, indicating the detection of carbon monoxide on the TNOs is likely to be trapped in the radiation-processed ice matrix (M. E. Brown & W. C. Fraser 2023; M. N. De Prá et al. 2024). Also, the difference at two temperatures of the  $^{13}\text{CO}$  to  $^{13}\text{CO}_2$  ratio implies this parameter is a possible correlation with specific environments on TNOs, such as temperature, radiation history, and geochemical evolution. H. Carrascosa et al. (2019) have also found that the nitrogen ( $\text{N}_2$ ) mixed in  $^{13}\text{CO}_2$  ice can change this constant because the presence of  $\text{N}_2$  can partially trap the photoproducts and therefore prevent two  $^{13}\text{CO}$  molecules from reforming  $^{13}\text{CO}_2$ . The temporal profile of ozone ( $\text{O}_3$ ) at both temperatures nearly overlaps in the first 2 hr and then decreases (Figure 3(c)). However, the decline at 40 K is faster than at 10 K, leading to two final column densities of  $3.0 \times 10^{16}$  and  $3.8 \times 10^{16}$  molecule cm $^{-2}$ , with branching ratios of about 9.7% and 17.1% (Table 3), respectively. The drop of  $\text{O}_3$  suggests the bond cleavage reaction with forming  $\text{O}_2$  and O as discussed before (C. J. Bennett et al. 2014; R. Martín-Doménech et al. 2015). The faster decrease at 40 K is likely because O atoms diffuse rapidly at higher temperatures, making the recombination process to form  $\text{O}_3$  less efficient. Both  $^{13}\text{CO}_3$  isomers have shown a trend of rapid accumulation followed by gradual decay during irradiation, but the 40 K ices exhibit a faster decrease (Figures 3(d) and (e)), suggesting the cleavage reaction for  $^{13}\text{CO}_3$  at 40 K is more efficient (C. S. Jamieson et al. 2006a). The final branching ratios for  $^{13}\text{CO}_3$  ( $C_{2v}$ ) at 40 and 10 K are 0.1% and 0.3%, correspondingly, for  $^{13}\text{CO}_3$  ( $D_{3h}$ ) are 0.1% and 0.1%. The evolution of  $^{13}\text{CO}_4$ ,  $^{13}\text{CO}_5$ , and  $^{13}\text{CO}_6$  products also presents an

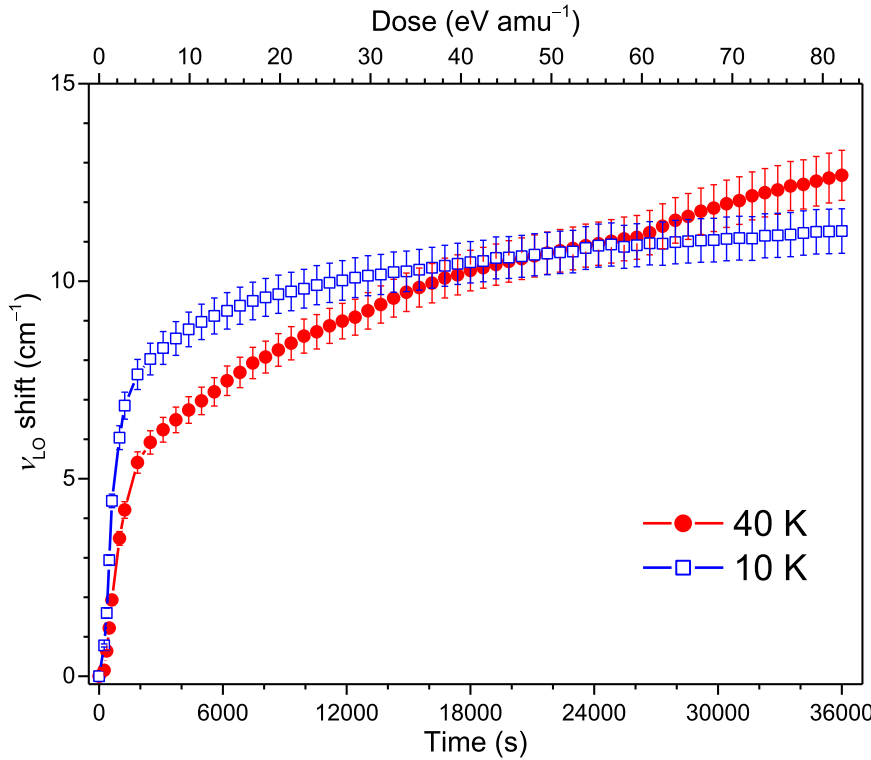


**Figure 2.** The evolution of redshift for the  $^{13}\text{CO}_2$  longitudinal optical (LO) phonon mode during irradiation at 40 and 10 K.

initial increase quickly followed by a decrease slowly (Figures 3(f)–(h)), and the declines at 40 K are faster than at 10 K. The  $^{13}\text{CO}_5$  and  $^{13}\text{CO}_6$  have similar branching ratios of 0.01% and 0.02% at 40 and 10 K, respectively. The amounts of  $^{13}\text{CO}_4$  are twice those of as  $^{13}\text{CO}_5$  and  $^{13}\text{CO}_6$  with branch ratios of 0.02% and 0.04% at corresponding temperatures.

Studies on high-energy electrons processed  $\text{CO}_2$  ices suggested that the dissociation of  $^{13}\text{CO}_2$  can result in the formation of  $^{13}\text{CO}$  and an oxygen atom (C. J. Bennett et al. 2004; C. S. Jamieson et al. 2006a; C. S. Jamieson et al. 2006b, 2007a, 2007b, 2008; D. V. Mifsud et al. 2022). The self-combination of suprathermal or thermalized oxygen atoms will produce molecular oxygen ( $\text{O}_2$ ). The addition of such oxygen atom to  $^{13}\text{CO}_2$  can produce  $^{13}\text{CO}_3$  ( $C_{2v}/D_{3h}$ ), and to  $\text{O}_2$  yields ozone ( $\text{O}_3$ ) via a barrierless reaction (C. J. Bennett & R. I. Kaiser 2005; B. Sivaraman et al. 2007). These reactions can also take place when  $\text{CO}_2$  ices are exposed to vacuum-ultraviolet (VUV) light irradiation (P. A. Gerakines et al. 1996; K. I. Öberg et al. 2009; D. A. Bahr & R. A. Baragiola 2012; R. Martín-Doménech et al. 2015; H. Carrascosa et al. 2019; N. E. Sie et al. 2019). The branching ratio of CO obtained in this study at 10 K agrees with that found in R. Martín-Doménech et al. (2015); however, that of  $\text{CO}_3$  is higher and  $\text{O}_3$  is lower than the VUV photons processed sample. The reaction channels from  $^{13}\text{CO}_2$  and electronically excited oxygen atom forming  $^{13}\text{CO}_3$  ( $C_{2v}$ ) and  $^{13}\text{CO}_3$  ( $D_{3h}$ ) are exoergic with energies of 197.5 and 197.1 kJ mol<sup>-1</sup>, respectively (C. J. Bennett et al. 2004). Note that the  $D_{3h}$  isomer may also be produced by isomerization of the  $C_{2v}$  structure and vice versa. Kinetic fits determined the rate constant ratio of Reactions (4)–(5) is about 7 (C. S. Jamieson et al. 2006a). This suggests that the  $^{13}\text{CO}_3$  ( $C_{2v}$ ) isomer is preferentially formed, which aligns with the temporal profiles in Figures 3(d) and (e).

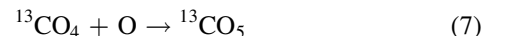
Namely, the column density of  $^{13}\text{CO}_3$  ( $C_{2v}$ ) reaches about  $6 \times 10^{14}$  molecule cm<sup>-2</sup> within 10 minutes, while  $^{13}\text{CO}_3$  ( $D_{3h}$ ) takes about 90 minutes to that value.



The formation of  $^{13}\text{CO}_4$  can either be through adding the oxygen atom to  $^{13}\text{CO}_3$  or the reaction between  $^{13}\text{CO}$  and  $\text{O}_3$ . However, the rate constant from kinetic fit for the former reaction was found to be negligible in comparison to the latter one (C. S. Jamieson et al. 2007a), suggesting  $^{13}\text{CO}_4$  molecules are mainly from the combination of products  $^{13}\text{CO}$  and  $\text{O}_3$ ,



The stepwise addition of oxygen atoms, Equations (7) and (8), generates  $^{13}\text{CO}_5$  and  $^{13}\text{CO}_6$  products (C. S. Jamieson et al. 2007a, 2008). These two processes are exoergic by 166.3 and 145.2 kJ mol<sup>-1</sup>, respectively, as calculated at the CCSD(T)/6-311+G\* level for the reactions of O ( $^3\text{P}$ ) and, correspondingly, by 356.1 and 335.1 kJ mol<sup>-1</sup> for the reactions of O ( $^1\text{D}$ ).



For the formation of  $^{13}\text{CO}_5$  and  $^{13}\text{CO}_6$  molecules, the oxygen atoms can either insert into an O–O or C–O single bond to expand the ring-oxygen structure in one step. Alternatively, the oxygen atom might interact with one of the ring-oxygen

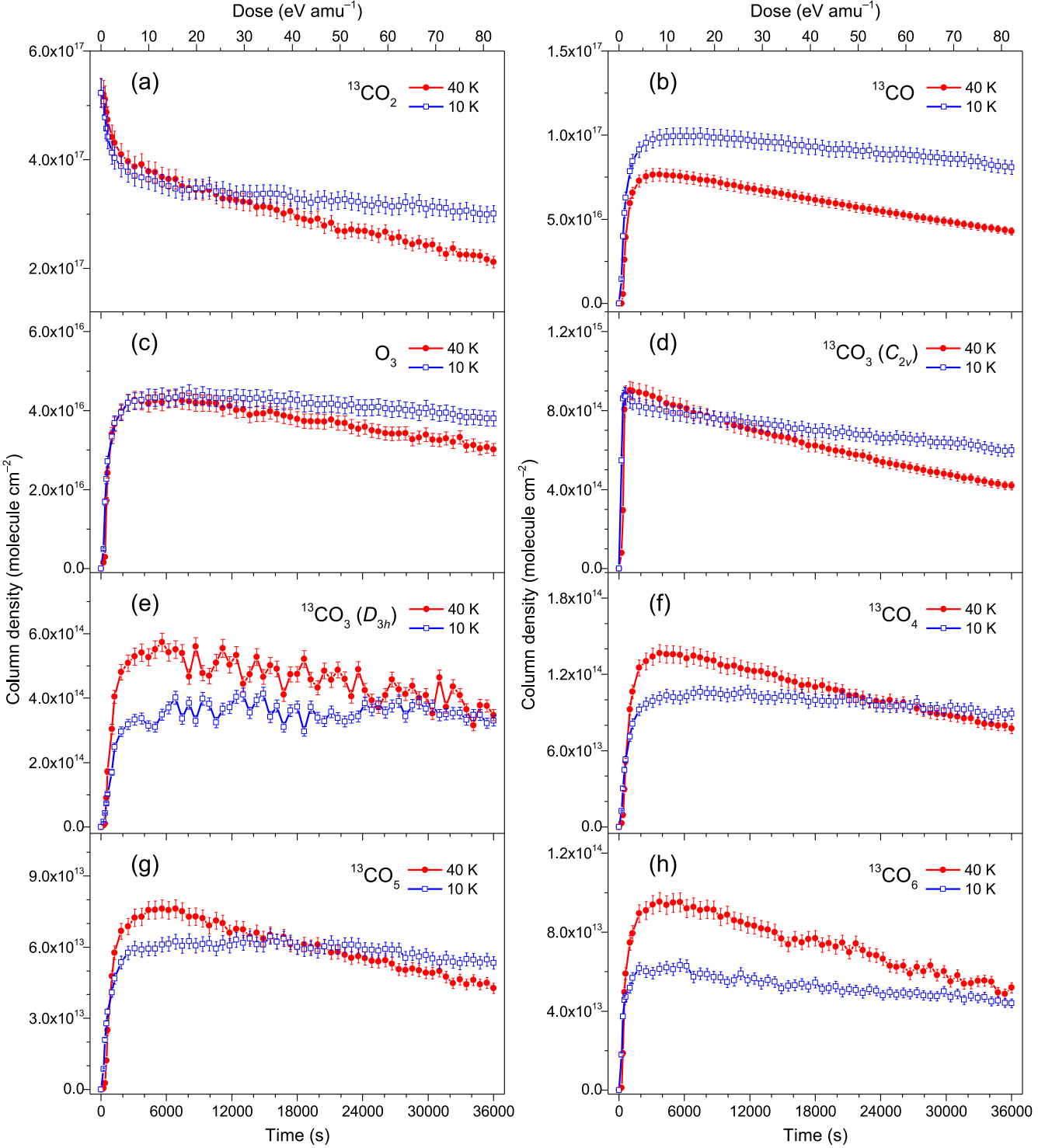


**Figure 3.** Temporal evolutions of the column densities for <sup>13</sup>CO<sub>2</sub> during the irradiation at 40 and 10 K along with identified products of <sup>13</sup>CO, O<sub>3</sub>, <sup>13</sup>CO<sub>3</sub> ( $C_{2v}$ / $D_{3h}$ ), <sup>13</sup>CO<sub>4</sub>, <sup>13</sup>CO<sub>5</sub>, and <sup>13</sup>CO<sub>6</sub>.

atoms to form an exocyclic O–O weak bond. It is worth noting that the latter mechanism has to follow a ring-opening process before completing the ring expansion, that is, via a two-step mechanism compared to a one-step insertion pathway (R. I. Kaiser & A. M. Mebel 2008). It is stressed that oxygen atoms might be then implanted into these ices to synthesize even higher-order carbon oxides, possibly <sup>13</sup>CO<sub>7</sub> and <sup>13</sup>CO<sub>8</sub> without a sufficient quantity as to be detected by infrared spectroscopy, but can be determined by a more sensitive

method such as photoionization reflectron time-of-flight mass spectrometry in the future.

#### 4. Conclusions and Astrophysical Implications

In summary, we conducted a systematic analysis of FTIR measurement of <sup>13</sup>CO<sub>2</sub> ices processed by GCR proxy under simulated TNO surface conditions. Our studies demonstrate that the GCR proxy exposure on <sup>13</sup>CO<sub>2</sub> ices at temperatures of

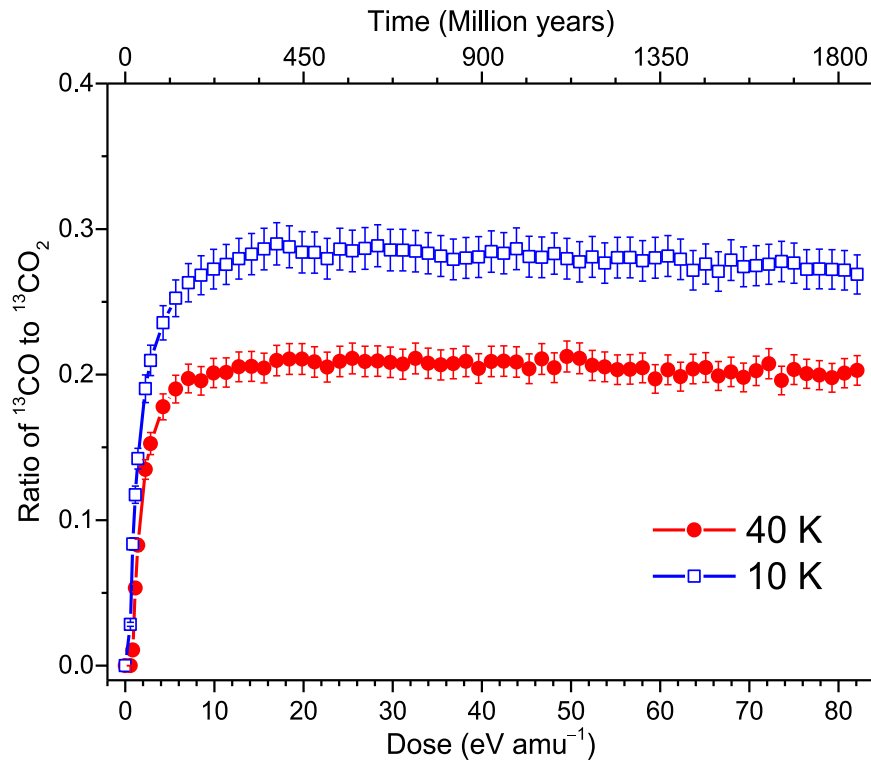


**Figure 4.** The evolution of the ratio between carbon monoxide ( $^{13}\text{CO}$ ) and carbon dioxide ( $^{13}\text{CO}_2$ ) during irradiation of  $^{13}\text{CO}_2$  at 40 and 10 K. All the values are calculated from column densities of corresponding molecules.

**Table 3**  
The Absorption Coefficients Used to Determine Column Densities of Molecules Identified within Irradiated  $^{13}\text{CO}_2$  Ices

Compound	Mode	Position (cm $^{-1}$ )	Absorption Coefficients (cm molecule $^{-1}$ )	References	Branching Ratio 40/10 K (%)
$^{13}\text{CO}_2$	$\nu_1 + \nu_3$	3629	$1.8 \times 10^{-18}$	M. Bouilloud et al. (2015)	...
$^{13}\text{CO}$	$\nu_1$	2094	$1.1 \times 10^{-17}$	M. Bouilloud et al. (2015)	13.8/36.4
$\text{O}_3$	$\nu_3$	1044	$1.5 \times 10^{-18}$	C. J. Bennett & R. I. Kaiser (2005)	9.7/17.1
$^{13}\text{CO}_3$ ( $C_{2v}$ )	$\nu_1$	1990	$8.9 \times 10^{-17}$	C. J. Bennett et al. (2004)	0.1/0.3
$^{13}\text{CO}_3$ ( $D_{3h}$ )	$\nu_1/\nu_2$	1136	$1.2 \times 10^{-17}$	C. J. Bennett et al. (2004)	0.1/0.1
$^{13}\text{CO}_4$	$\nu_1$	1895	$1.0 \times 10^{-16}$	C. S. Jamieson et al. (2007b)	0.02/0.04
$^{13}\text{CO}_5$	$\nu_1$	1874	$8.0 \times 10^{-17}$	C. S. Jamieson et al. (2007a)	0.01/0.02
$^{13}\text{CO}_6$	$\nu_1$	1841	$5.5 \times 10^{-17}$	C. S. Jamieson et al. (2008)	0.02/0.02

**Note.** The absorption coefficients of  $\text{O}_3$ ,  $^{13}\text{CO}_3$ ,  $^{13}\text{CO}_4$ ,  $^{13}\text{CO}_5$ , and  $^{13}\text{CO}_6$  are from theoretical calculations.

40 and 10 K leads to the formation of several radiolysis products, including  $^{13}\text{CO}$ ,  $\text{O}_3$ ,  $^{13}\text{CO}_3$  ( $C_{2v}/D_{3h}$ ),  $^{13}\text{CO}_4$ ,  $^{13}\text{CO}_5$ , and  $^{13}\text{CO}_6$ . Acquired spectra in the  $\nu_3$ -region present complex features, including LO phonon signals and crystalline and amorphous  $^{13}\text{CO}_2$  components. The evolution of spectra depicts notable redshifts of the LO features during the irradiation. We also found that all products show a tendency of initial rapid increases followed by gradual decreases with extended irradiation, and the decrease at 40 K is faster than at 10 K. In addition, the ratio between  $^{13}\text{CO}$  and  $^{13}\text{CO}_2$  increases to constant values of 0.20 at 40 K and 0.27 at 10 K as the radiation dose accumulates, which has potential implications for understanding the physical environment and the retention of volatile carbon monoxide on TNOs.

The irradiation experiments of  $^{13}\text{CO}_2$  ices, which simulate the chemical evolution of  $\text{CO}_2$ -rich TNOs' surface processed by GCRs, presented here are directly relevant to the

astrochemistry of solar system ices and ice-covered interstellar dust, regarding that this isotopically labeled molecule has a high abundance in deep space (M. K. McClure et al. 2023; N. G. C. Brunken et al. 2024; M. N. De Prá et al. 2024) and continues bombardment by a variety of radiation sources such as GCRs and SWs (R. E. Johnson 1990; R. I. Kaiser & K. Roessler 1997; R. Hudson et al. 2008; C. J. Bennett et al. 2013; R. Métayer et al. 2019). First, products from processed  $^{13}\text{CO}_2$  ices, such as  $^{13}\text{CO}_3$  and  $\text{O}_3$ , give potential detectable molecules in the trans-Neptunian region by telescopes like JWST (R. Métayer et al. 2019; B. C. Ferrari et al. 2021). Also, the production and retention of  $^{13}\text{CO}$  at 40 K provide a plausible source for carbon monoxide observed on TNOs, which is consistent with the pattern that the JWST only detects CO on the TNOs with more abundant  $\text{CO}_2$  (M. E. Brown & W. C. Fraser 2023; M. N. De Prá et al. 2024). Second, the radiation dose used here corresponds to approximately 1.8

billion yr of GCR exposure on the top several hundred nanometers of a TNO surface (J. F. Cooper et al. 2003; G. Strazzulla et al. 2003; R. Hudson et al. 2008). Through scaling the irradiation time here to the surface of a TNO, the kinetic profiles of processed  $^{13}\text{CO}_2$  along with products offer potential applications for testing the  $\text{CO}_2$ -bearing chemical model of TNOs and serving as a tracer for specific environments in the outer solar system (D. Fulvio et al. 2012; T. Pauly & R. T. Garrod 2018; C. Ahrens et al. 2022). Moreover, the behavior of solid-state  $\text{CO}_2$  can also be used to trace the differences in carbon sources induced by geological activity on carbon-rich moons such as Europa and Callisto (S. K. Trumbo & M. E. Brown 2023; G. L. Villanueva et al. 2023; R. J. Cartwright et al. 2024b). The redshift of  $^{13}\text{CO}_2$  LO phonon mode observed here may contribute to the astronomical observation of TNOs, considering the light source (Sun) has various incidence angles with their surfaces, and can also provide information on the morphology, irradiation history, and ice composition (R. M. Escribano et al. 2013; I. R. Cooke et al. 2016; R. J. Cartwright et al. 2024a). In addition, as mentioned above,  $\text{CO}_2$  and  $\text{CO}$  are widespread compounds in the trans-Neptunian space with a strong correlation in abundance (M. N. De Prá et al. 2024) and the relative amount between them can be linked to specific conditions on a TNO. Therefore, the ratio of  $^{13}\text{CO}$  to  $^{13}\text{CO}_2$  obtained at different temperatures is expected to be involved in interpreting the observed relation between these two molecules on TNOs and reconstructing the GCR exposure history of TNOs or related astrophysical scenarios rich in carbon dioxide and carbon monoxide (S. Ioppolo et al. 2013b; M. K. McClure et al. 2023; S. P. D. Birch & O. M. Umurhan 2024; N. G. C. Brunken et al. 2024; S. Faggi et al. 2024; A. C. Souza-Feliciano et al. 2024).

### Acknowledgments

We acknowledge support from NASA grant 80NSSC21K1834 and 80NSSC24K1732.

### ORCID iDs

Chaojiang Zhang  <https://orcid.org/0000-0003-3727-901X>  
 Leslie A. Young  <https://orcid.org/0000-0002-7547-3967>  
 Ralf I. Kaiser  <https://orcid.org/0000-0002-7233-7206>

### References

- Abplanalp, M. J., Förstel, M., & Kaiser, R. I. 2016, *CPL*, 644, 79  
 Ahrens, C., Meraviglia, H., & Bennett, C. 2022, *Geosc*, 12, 51  
 Allodi, M. A., Ioppolo, S., Kelley, M. J., McGuire, B. A., & Blake, G. A. 2014, *PCCP*, 16, 3442  
 Bahr, D. A., & Baragiola, R. A. 2012, *ApJ*, 761, 36  
 Baratta, G. A., & Palumbo, M. E. 1998, *JOSAA*, 15, 3076  
 Baratta, G. A., & Palumbo, M. E. 2017, *A&A*, 608, A81  
 Bennett, C. J., Ennis, C. P., & Kaiser, R. I. 2014, *ApJ*, 794, 57  
 Bennett, C. J., Jamieson, C., Mebel, A. M., & Kaiser, R. I. 2004, *PCCP*, 6, 735  
 Bennett, C. J., Jamieson, C. S., & Kaiser, R. I. 2009a, *ApJS*, 182, 1  
 Bennett, C. J., Jamieson, C. S., & Kaiser, R. I. 2009b, *PCCP*, 11, 4210  
 Bennett, C. J., Jamieson, C. S., & Kaiser, R. I. 2010, *PCCP*, 12, 4032  
 Bennett, C. J., Jamieson, C. S., Osamura, Y., & Kaiser, R. I. 2005, *ApJ*, 624, 1097  
 Bennett, C. J., & Kaiser, R. I. 2005, *ApJ*, 635, 1362  
 Bennett, C. J., Pirim, C., & Orlando, T. M. 2013, *ChRv*, 113, 9086  
 Bernstein, M., Cruikshank, D., & Sandford, S. 2005, *Icar*, 179, 527  
 Birch, S. P. D., & Umurhan, O. M. 2024, *Icar*, 413, 116027  
 Boogert, A. C. A., Ehrenfreund, P., Gerakines, P. A., et al. 2000, *A&A*, 353, 349  
 Boogert, A. C. A., Gerakines, P. A., & Whittet, D. C. B. 2015, *ARA&A*, 53, 541  
 Bouilloud, M., Fray, N., Bénilan, Y., et al. 2015, *MNRAS*, 451, 2145  
 Brown, M. E., & Fraser, W. C. 2023, *PSJ*, 4, 130  
 Brunken, N. G. C., Rocha, W. R. M., van Dishoeck, E. F., et al. 2024, *A&A*, 685, A27  
 Carrascosa, H., Hsiao, L. C., Sie, N. E., Muñoz Caro, G. M., & Chen, Y. J. 2019, *MNRAS*, 486, 1985  
 Cartwright, R. J., Holler, B. J., Grundy, W. M., et al. 2024a, *ApJL*, 970, L29  
 Cartwright, R. J., Nordheim, T. A., DeColibus, R. A., et al. 2022, *PSJ*, 3, 8  
 Cartwright, R. J., Villanueva, G. L., Holler, B. J., et al. 2024b, *PSJ*, 5, 60  
 Cooke, I. R., Fayolle, E. C., & Öberg, K. I. 2016, *ApJ*, 832, 5  
 Cooper, J. F., Christian, E. R., Richardson, J. D., & Wang, C. 2003, *EM&P*, 92, 261  
 Crandall, P. B., Gillis-Davis, J. J., & Kaiser, R. I. 2019, *ApJ*, 887, 27  
 Dartois, E., Noble, J. A., Ysard, N., Demyk, K., & Chabot, M. 2022, *A&A*, 666, A153  
 De Prá, M. N., Hénault, E., Pinilla-Alonso, N., et al. 2024, *NatAs*, in press  
 D'Hendecourt, L. B., Jourdain, & de Muizon, M. 1989, *A&A*, 223, L5  
 Drouin, D., Couture, A. R., Joly, D., et al. 2007, *Scanning*, 29, 92  
 Ehrenfreund, P., Boogert, A. C. A., Gerakines, P. A., Tielens, A. G. G. M., & van Dishoeck, E. F. 1997, *A&A*, 328, 649  
 Emery, J. P., Wong, I., Brunetto, R., et al. 2024, *Icar*, 414, 116017  
 Escribano, R. M., Muñoz Caro, G. M., Cruz-Díaz, G. A., Rodríguez-Lazcano, Y., & Mate, B. 2013, *PNAS*, 110, 12899  
 Faggi, S., Villanueva, G. L., McKay, A., et al. 2024, *NatAs*, 8, 1237  
 Falk, M. 1987, *JChPh*, 86, 560  
 Ferrari, B. C., Slaviceinska, K., & Bennett, C. J. 2021, *Acc. Chem. Res.*, 54, 1067  
 Förstel, M., Maksyutenko, P., Mebel, A. M., & Kaiser, R. I. 2016, *ApJL*, 818, L30  
 Fulvio, D., Raut, U., & Baragiola, R. A. 2012, *ApJL*, 752, L33  
 Gerakines, P. A., & Hudson, R. L. 2015, *ApJL*, 808, L40  
 Gerakines, P. A., Schutte, W. A., & Ehrenfreund, P. 1996, *A&A*, 312, 289  
 Gomis, O., & Strazzulla, G. 2005, *Icar*, 177, 570  
 Grant, S. L., van Dishoeck, E. F., Tabone, B., et al. 2023, *ApJL*, 947, L6  
 Hacquard, A. B., Torres-Díaz, D., Basalgète, R., et al. 2024, *PCCP*, 26, 18741  
 He, J., Emtiaz, S. M., Boogert, A., & Vidali, G. 2018, *ApJ*, 869, 41  
 He, J., & Vidali, G. 2018, *MNRAS*, 473, 860  
 Hudson, R., Palumbo, M. E., Strazzulla, G., et al. 2008, in *The Solar System beyond Neptune*, ed. M. A. Barucci et al. (1st ed.; Arizona: Univ. Arizona Press), 507  
 Ioppolo, S., Fedoseev, G., Lamberts, T., Romanzin, C., & Linnartz, H. 2013a, *RSCl*, 84, 073112  
 Ioppolo, S., Sangiorgio, I., Baratta, G. A., & Palumbo, M. E. 2013b, *A&A*, 554, A34  
 Ishibashi, A., Molpeceres, G., Hidaka, H., et al. 2024, *ApJ*, 976, 162  
 Isokoski, K., Poteet, C. A., & Linnartz, H. 2013, *A&A*, 555, A85  
 Jamieson, C. S., Mebel, A. M., & Kaiser, R. I. 2006a, *ChemPhysChem*, 7, 2508  
 Jamieson, C. S., Mebel, A. M., & Kaiser, R. I. 2006b, in *AIP Conf. Proc., Astrochemistry: From Laboratory Studies to Astronomical Observations* 855 (Melville, NY: AIP), 100  
 Jamieson, C. S., Mebel, A. M., & Kaiser, R. I. 2006c, *ApJS*, 163, 184  
 Jamieson, C. S., Mebel, A. M., & Kaiser, R. I. 2007a, *CPL*, 443, 49  
 Jamieson, C. S., Mebel, A. M., & Kaiser, R. I. 2007b, *CPL*, 440, 105  
 Jamieson, C. S., Mebel, A. M., & Kaiser, R. I. 2008, *CPL*, 450, 312  
 Jheeta, S. 2014, *Orient. J. Chem.*, 30, 401  
 Johnson, R. E. 1990, *Energetic Charged-Particle Interactions with Atmospheres and Surfaces* (1st ed.; Springer: Springer)  
 Johnson, R. E. 1991, *JGRE*, 96, 17553  
 Jones, B. M., & Kaiser, R. I. 2013, *JPCL*, 4, 1965  
 Kaiser, R. I., & Mebel, A. M. 2008, *CPL*, 465, 1  
 Kaiser, R. I., & Roessler, K. 1997, *ApJ*, 475, 144  
 Keane, J. V., Boogert, A. C. A., Tielens, A. G. G. M., Ehrenfreund, P., & Schutte, W. A. 2001, *A&A*, 375, L43  
 Kim, Y. S., & Kaiser, R. I. 2012, *ApJ*, 758, 37  
 Kleimeier, N. F., Liu, Y., Turner, A. M., et al. 2022, *PCCP*, 24, 1424  
 Martín-Doménech, R., Manzano-Santamaría, J., Muñoz Caro, G. M., et al. 2015, *A&A*, 584, A14  
 Maté, B., Gálvez, O., Martín-Llorente, B., et al. 2008, *JPhChA*, 112, 457  
 McClure, M. K., Rocha, W. R. M., Pontoppidan, K. M., et al. 2023, *NatAs*, 7, 431  
 Mejía, C., Bender, M., Severin, D., et al. 2015, *NIMPB*, 365, 477  
 Mennella, V., Baratta, G. A., Palumbo, M. E., & Bergin, E. A. 2006, *ApJ*, 643, 923

- Mennella, V., Palumbo, M. E., & Baratta, G. A. 2004, *ApJ*, **615**, 1073  
 Menten, S. M., Sori, M. M., & Bramson, A. M. 2022, *NatCo*, **13**, 4457  
 Métayer, R., Guilbert-Lepoutre, A., Ferruit, P., et al. 2019, *FrASS*, **6**, 8  
 Mifsud, D. V., Kaňuchová, Z., Ioppolo, S., et al. 2022, *JMoSp*, **385**, 111599  
 Minissale, M., Congiu, E., Manicò, G., Pirronello, V., & Dulieu, F. 2013, *A&A*, **559**, A49  
 Minissale, M., Loison, J. C., Baouche, S., et al. 2015, *A&A*, **577**, A2  
 Molpeceres, G., Enrique-Romero, J., & Aikawa, Y. 2023, *A&A*, **677**, A39  
 Nayak, O., Hirschauer, A. S., Kavanagh, P. J., et al. 2024, *ApJ*, **963**, 94  
 Noble, J. A., Fraser, H. J., Smith, Z. L., et al. 2024, *NatAs*, **8**, 1169  
 Oba, Y., Watanabe, N., Kouchi, A., Hama, T., & Pirronello, V. 2010, *ApJL*, **712**, L174  
 Öberg, K. I., Fraser, H. J., Boogert, A. C. A., et al. 2007, *A&A*, **462**, 1187  
 Öberg, K. I., van Dishoeck, E. F., & Linnartz, H. 2009, *A&A*, **496**, 281  
 Osberg, W. E., & Hornig, D. F. 1952, *JChPh*, **20**, 1345  
 Ovchinnikov, M. A., & Wight, C. A. 1993, *JChPh*, **99**, 3374  
 Pauly, T., & Garrod, R. T. 2018, *ApJ*, **854**, 13  
 Quirico, E., Bacmann, A., Wolters, C., et al. 2023, *Icar*, **394**, 115396  
 Raut, U., & Baragiola, R. A. 2013, *ApJ*, **772**, 53  
 Raut, U., Fulvio, D., Loeffler, M. J., & Baragiola, R. A. 2012, *ApJ*, **752**, 159  
 Rodriguez-Garcia, V., Hirata, S., Yagi, K., et al. 2007, *JChPh*, **126**, 124303  
 Sabri, T., Baratta, G. A., Jäger, C., et al. 2015, *A&A*, **575**, A76  
 Sandford, S. A., & Allamandola, L. J. 1990, *ApJ*, **355**, 357  
 Satorre, M. A., Palumbo, M. E., & Strazzulla, G. 2000, *Ap&SS*, **274**, 643  
 Sie, N. E., Caro, G. M. M., Huang, Z. H., et al. 2019, *ApJ*, **874**, 35  
 Sivaraman, B., Jamieson, C. S., Mason, N. J., & Kaiser, R. I. 2007, *ApJ*, **669**, 1414  
 Sivaraman, B., Raja Sekhar, B. N., Fulvio, D., et al. 2013, *JChPh*, **139**, 074706  
 Souza-Feliciano, A. C., Holler, B. J., Pinilla-Alonso, N., et al. 2024, *A&A*, **681**, L17  
 Strazzulla, G., Cooper, J. F., Christian, E. R., & Johnson, R. E. 2003, *CRPhy*, **4**, 791  
 Trumbo, S. K., & Brown, M. E. 2023, *Sci*, **381**, 1308  
 Turner, A. M., Abplanalp, M. J., Chen, S. Y., et al. 2015, *PCCP*, **17**, 27281  
 Turner, A. M., & Kaiser, R. I. 2020, *AcChR*, **53**, 2791  
 Villanueva, G. L., Hammel, H. B., Milam, S. N., et al. 2023, *Sci*, **381**, 1305  
 Vogt, J. 2024, *PCCP*, **26**, 21019  
 Young, L. A., Braga-Ribas, F., & Johnson, R. E. 2020, in The Trans-Neptunian Solar System, ed. D. Prialnik, M. A. Barucci, & L. A. Young (1st ed.; Amsterdam: Elsevier), 127  
 Yuan, C., Cooke, I., & R. Yates, J. T. 2014, *ApJL*, **791**, L21  
 Yuan, C., & Yates, J. T. 2013, *ApJ*, **780**, 8  
 Zhang, C., Leyvac, V., Wang, J., et al. 2024, *PNAS*, **121**, e2320215121  
 Zheng, W., Jewitt, D., Osamura, Y., & Kaiser, R. I. 2008, *ApJ*, **674**, 1242  
 Zins, E-L., Joshi, P. R., & Krim, L. 2011, *ApJ*, **738**, 175